



## Non-invasive local pulse wave velocity using 4D-flow MRI

Joaquín Mura<sup>a,b,h,\*</sup>, Julio Sotelo<sup>b,c,f,h</sup>, Hernán Mella<sup>b,f,h</sup>, James Wong<sup>d</sup>, Tarique Hussain<sup>e,d</sup>, Bram Ruijsink<sup>d</sup>, Sergio Uribe<sup>b,f,g,h</sup>

<sup>a</sup> Department of Mechanical Engineering, Universidad Técnica Federico Santa María, Santiago, Chile

<sup>b</sup> Biomedical Imaging Center, Pontificia Universidad Católica de Chile, Santiago, Chile

<sup>c</sup> School of Biomedical Engineering, Universidad de Valparaíso, Valparaíso, Chile

<sup>d</sup> Imaging and Biomedical Engineering, King's College of London, London, United Kingdom

<sup>e</sup> Pediatric Cardiology, University of Texas Southwestern Medical Center, Dallas, TX, USA

<sup>f</sup> Department of Electrical Engineering, School of Engineering, Pontificia Universidad Católica de Chile, Santiago, Chile

<sup>g</sup> Department of Radiology, Faculty of Medicine, Pontificia Universidad Católica de Chile, Santiago, Chile

<sup>h</sup> Millennium Nucleus in Cardiovascular Magnetic Resonance, Cardio MR, Chile

### ARTICLE INFO

#### Keywords:

Pulse Wave Velocity  
Arterial Stiffness  
Cardiac diseases  
4D-Flow MRI

### ABSTRACT

Pulse Wave Velocity (PWV) corresponds to the velocity at which pressure waves, generated by the systolic contraction in the heart, propagate along the arterial tree. Due to the complex interplay between blood flow and the artery wall, PWV is related to inherent mechanical properties and arterial morphology. PWV has been widely accepted as a biomarker and early predictor to evaluate global arterial distensibility. Still, several local abnormalities often remain hidden or difficult to detect using non-invasive techniques. Here, we introduce a novel method to efficiently construct a local estimate of PWV along the aorta using 4D-Flow MRI data. A geodesic distance map was used to track advancing pulses for efficient flow calculations, based on the observation that the propagation of velocity wavefronts strongly depends on the arterial morphology. This procedure allows us a robust evaluation of the local transit time due to the pulse wave at each position in the aorta. Moreover, the estimation of the local PWV map did not require centerlines, and the final result is projected back to 3D using the same geodesic map. We evaluated PWV values in healthy young and adult volunteers and patients with uni-ventricular physiology after a Fontan procedure. Our method is fast, semi-automatic, and depicts differences between young versus adult volunteers and young volunteers versus Fontan patients, showing consistent results compared to global methods. Remarkably, the technique could detect local differences of PWV on the aortic arch for all subjects, being consistent with previous findings of reduced PWV in the aortic arch.

### 1. Introduction

Non-invasive biomarkers for cardiovascular diseases are an intensive research subject due to their implications: Patient safety and less expensive examinations. In that direction, cardiologists have introduced several ways to detect abnormalities by means of different cardiac imaging modalities, to provide qualitative and quantitative information about the performance of the cardiovascular system. One of them is Computed Tomography Angiography (CTA), which, jointly with computational fluid dynamics, can infer Fractional-Flow Reserve (FFR) across the stenosis in coronary arteries [1]. Another recent approach for FFR is [2], in which Machine Learning is used to approach blood flow from static CTA. However, the 4D-Flow MRI technique has gained

interest because it may reveal valuable data for assessing the hemodynamics in heart chambers and large vessels [3–5]. The development of 4D-Flow has enabled the computation of non-invasive cardiovascular parameters beyond FFR, including wall shear stress, helicity, vorticity, viscous dissipation, oscillatory shear index, among others. These new parameters have already shown promising results in different cardiovascular pathologies [4,6–8].

Another relevant biomarker is the aortic Pulse Wave Velocity (PWV), corresponding to the speed of pressure waves propagated along the arterial tree, generated by the systolic contraction in the heart. The standard technique for calculating PWV, particularly in the aorta, is through pressure data from cardiac catheterization. Nevertheless, that is an invasive procedure, operator skill dependent, it is also subjected to

\* Corresponding author at: Department of Mechanical Engineering, Universidad Técnica Federico Santa María, Santiago, Chile.

E-mail address: [joaquin.mura@usm.cl](mailto:joaquin.mura@usm.cl) (J. Mura).

<https://doi.org/10.1016/j.bspc.2021.103259>

Received 13 June 2020; Received in revised form 22 September 2021; Accepted 15 October 2021

Available online 23 October 2021

1746-8094/© 2021 Elsevier Ltd. All rights reserved.

the positioning of the catheters and not free of complications [9–10]. Another approach to obtain PWV is by flow calculations. From Navier-Stokes equations in cylindrical coordinates, it follows that pressure and flow propagate at the same wave velocity (see [11]; hence, either pressure or flow data can be considered to calculate PWV.

Utilizing non-invasive techniques for PWV offers a new paradigm to evaluate biomechanical markers for several aortic diseases [12]. A standard procedure for registering pulse waves is the transcutaneous tonometer by compressing superficial arteries [13–14]. Similar to ultrasound imaging, it is beneficial in many fields, including the calculation of PWV, but still restricted to small and near-surface vessels (see [15–16]). Moreover, the limited number of regions that can be measured, inter-operator variability, and incertitude in the position of sensors [17–18] make detecting local alterations difficult.

Besides theoretical formulations made for straight pipes (see, e.g. [19–21]), PWV in the aorta can be calculated as the quotient  $PWV = \Delta d / \Delta t$ , where  $\Delta d$  is the arc length between two reference points and  $\Delta t$  is the time delay (or transit time) of the wave. Therefore, the global calculation of PWV in the aorta requires one point in the ascending and another in the descending aorta. The time-delay is obtained by comparing flow, velocity, or pressure curves between these two specific points.

Methods such as 2D or 3D CINE phase-contrast (PC) MRI, also known as 4D-Flow MRI [9], have been used to obtain global PWV. Two-dimensional flow evaluations [22], or distensibility measures [23], although useful and reliable, may still require multiple slice locations to assess PWV in different regions, as suggested by [24]. However, the planning of several slices may be tedious and time-consuming to truly assess regional PWV [10]. On the other hand, current methods based on 4D-Flow MRI data require calculating a centerline either selecting points or generating them semi-automatically using libraries as the Vascular Modeling Toolkit (*VMTK: The Vascular Modeling Toolkit is available at [www.vmtk.org](http://www.vmtk.org)*). Then, global PWV is obtained by adjusting a linear regression using the collected time-delay data [9]. This approach may be inaccurate in intricate geometries where flow or pressure wavefront does not necessarily coincide with the centerline.

In summary, there are some drawbacks in current procedures for estimating PWV, including:

- (a) The data collected by catheterization procedures are sensitive to correct catheter placement. It is also a risky procedure for patients.
- (b) The centerline methods do not necessarily coincide with the path followed by a wavefront. This misfit implies that, in such cases, distance and time calculated from flow curves may not be accurate.
- (c) Finally, current methods only provide global measurements of PWV.

To overcome these issues, we propose a novel and robust technique that considers the morphology to efficiently calculate flows, time-delays, and a continuous PWV map along the artery in a semi-automated manner.

## 2. Materials and methods

### 2.1. Morphology and flow preprocessing

We use two different datasets in this work: Fluid-Structure Interaction (FSI) simulations and DICOM files from MR scanners with 4D-Flow MR encoding. For the 3D FSI simulations, the geometries shown in Figs. 1 and 3 were generated using GMSH [25] (see the appendix for mesh details). In the case of DICOM files, the volume occupied by the fluid was segmented using a homemade Matlab library (The MathWorks, Natick, MA, USA), including the generation of the tetrahedral mesh, as detailed in previous reports in [7–8]. For the 4D Flow MRI data processing, the angiographic segmentation used: thresholding, labeling, and manual separation of the vessels [26]. The mesh, created using the iso2mesh MATLAB toolbox [27] and CGAL (Computational Geometry Algorithms Library, <http://www.cgal.org>), has nodal velocity values transferred from the 4D Flow MRI data sets using cubic interpolation.

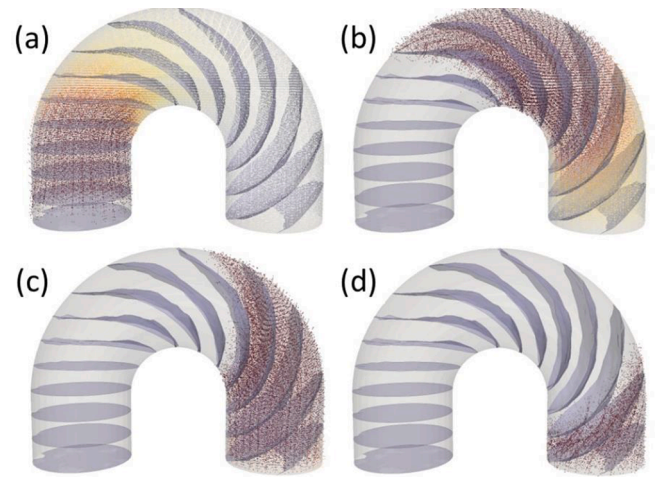


**Fig. 1.** From (a) to (d), four instants in Fluid-Structure simulation for a bent pipe, where an impulsive flow thrust the particles towards the outlet. The geodesic map displayed as level sets show that the wavefront does not follow a flat surface. The level set of the geodesic map appear like a good approximation to track wavefronts.

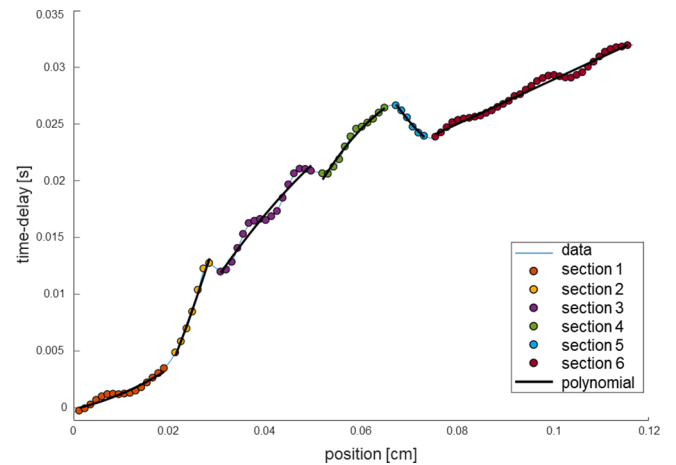


**Fig. 2.** Time-delay curve from a patient, where the color of balloons denotes different sections, and each one was fitted using a polynomial of degree 2 and a maximum of 6 segments.

This procedure permits the evaluation of flow at each node of a static and tetrahedral mesh, which facilitates calculating the quantities described below.

### 2.2. Geodesic distance map from the inlet

The propagation of waves in straight vessels has been widely analyzed in fluid mechanics literature [11]. Regardless of boundary effects, wavefronts can be characterized using parallel planes perpendicular to the symmetry axis in straight vessels [10,28]. For curved arteries, many studies have assumed that wavefronts are still planes perpendicular to the axis of symmetry, which may not necessarily be true [29].

To estimate the shape of wavefronts, we proposed to use the geodesic distance from a given source. According to Fermat's principle (i.e., the shortest travel time gives the best path to evaluate distances), any wavefront was recovered as the level-set in the distance map over the region of interest. The formulation of the distance problem (known as Eikonal) was to find  $d : \Omega \subset \mathbb{R}^3 \rightarrow \mathbb{R}$  solution to

$$\|\nabla d\| = 1 \text{ in } \Omega, d = 0 \text{ on } \Gamma \quad (1)$$

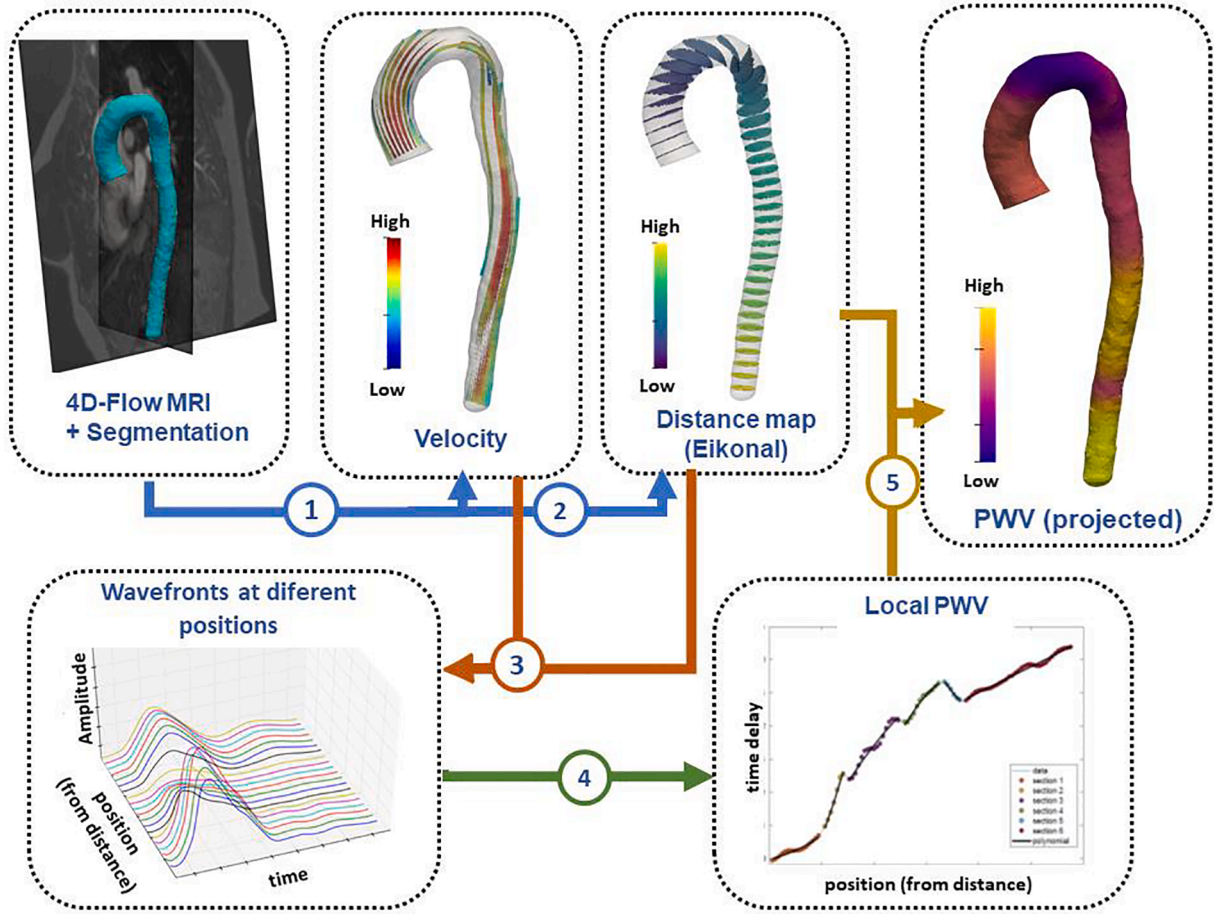


**Fig. 3.** Schematic description of the method. (1)The acquisition images are encoded with 4D-Flow MRI, leading to the segmentation as a tetrahedral mesh. The velocity is interpolated to the mesh. (2) The Eikonal solver on the mesh provides the distance map (with respect to the inlet). (3) Velocity and distance map permit the calculation of the wavefronts. (4) Time delay is recovered using a robust cross-correlation between the wavefronts. Its expected value is localized in the artery with the distance map. Hence, PWV is estimated from the monotonic slope filtering. (5) Finally, the PWV is projected on the mesh using the distance map.

With  $\|y\| = \sqrt{\sum_{i=1}^3 y_i^2}$  for any  $y \in \mathbb{R}^3$  [30]. The domain  $\Omega$  was the region of interest, and  $\Gamma$  represented the reference surface, i.e., the inlet.

The numerical solution of the nonlinear hyperbolic equation (1) was obtained using the Fast Sweeping (FS) method over tetrahedral meshes, as proposed in [31]. The algorithm, implemented in C++, produced fast and accurate solutions with a complexity of  $O(N \log N)$  (where  $N$  was the number of nodes in the tetrahedral mesh). The normal vector to the level set  $d = \text{constant}$ , for any  $\epsilon \in \Omega$ , was defined as

$$n(x) = \frac{\nabla d(x)}{\|\nabla d(x)\|} \quad (2)$$

The definition given in (2) produced an extrapolation of the normal vector to every point in  $\Omega$ . In Fig. 1, one example of the wavefront evolution is where the FSI model illustrates how a pulse wave produced at the inlet propagates towards the outlet (see section 2.4). In that figure, the geodesic map obtained as the numerical solution to the Eikonal problem (1) showed that level-sets are an excellent approximation to follow wavefronts and propagation of pulses.

### 2.3. Time delay estimation

The time delay can be estimated via transit-time, flow-area, or cross-correlation methods. Transit-time and cross-correlation methods produce similar and reproducible results, while flow-area requires more intensive user interaction (see [32]. Although transit-time methods, like time-to-foot, are robust and comparable to cross-correlation (7). The

latter can be easily automated, and therefore, we have used this approach.

Before calculating cross-correlations between flow curves, we addressed some issues to estimate time delays as we explain below. These issues were related to (a) Backward flows and wave reflections, (b) the high computational cost of flow evaluations (at several locations), (c) temporal resolution, and noise sensitivity.

(a) Given  $n_p$  level-sets, we defined  $\Gamma_i = \{x \in \Omega \text{ such that } d(x) = l_i\}$  for a constant level  $0 \leq l_i \leq \max_x d(x)$  with  $i = 1, \dots, n_p$ , and the distance map  $d : \Omega \rightarrow \mathbb{R}$  solution to (1). As pointed out in [33], the site of wave reflections varies with age, making it difficult to predict which slices will be more affected by waves traveling from the periphery back to the heart. Therefore, due to Eq (2), the evaluation of the forward flow on the surface  $\Gamma_i$  is, for some fixed  $i$ , was

$$\llbracket v \cdot n \rrbracket^+ = \max(0, v \cdot n)$$

This filtering procedure gives us relevant information to capture forward pulses along the aorta.

(b) The flow was evaluated on several level-sets using the following integral identity

$$\int_{\Gamma_i} \llbracket v \cdot n \rrbracket^+ ds = \int_{\Omega} \llbracket v \cdot n \rrbracket^+ \delta_{\Gamma_i}(x) dx$$

reducing computational efforts. That was done to replace the explicit surface construction by an implicit level-set on the distance map, where  $\delta_{\Gamma}$  represents the Dirac mass over the subset  $\Gamma \subset \Omega$ . Since Dirac masses

cannot be numerically evaluated, the regularized version

$$\int_{\Gamma_i} \llbracket v \cdot n \rrbracket^+ ds = \int_{\Omega} \llbracket v \cdot n \rrbracket^+ w(x, l_i) dx \quad (3)$$

where  $w(x, l_i) = \delta_\epsilon(d(x) - l_i) |\nabla d|(x)$  and  $\delta_\epsilon(f) = \frac{\sqrt{\pi}}{3\epsilon} \exp\left(-\left(\frac{f}{3\epsilon}\right)^2\right)$  is an approximation to the Dirac mass for some  $0 < \epsilon \ll 1$ . We used  $\epsilon \approx 1.25 \times$  (mesh size), as proposed in [34]. Hence, for each level set, the time-delay curve is recovered with the implicit integration (3) for each time step.

- (c) Due to the range of PWV values in arteries oscillated between 2 and 15 [m/s] (see [21]), the temporal resolution was increased. Also, since time-delay, obtained from cross-correlations between waveforms, was sensitive to noise and the chosen interpolation, we introduced perturbations to produce more robust results. Instead of standard interpolation using polynomials or cubic splines, which are prone to overshoot with noisy data, we consider curve fitting using Fourier series for each waveform, considering 6,7,8,9,10,11 and 12 Fourier terms to generate seven independent curve reconstructions. Gaussian noise was added twice, to perturb the flow data with an amplitude of 5 % of the maximal velocity. Finally, the value obtained from cross-correlations among all the combinations, considering seven and fourteen, without and with noise, respectively, lead to a stable evaluation of the time-delay curve at several positions along the artery.

The numerical algorithms described above were implemented in Matlab (MATLAB Release 2018a and Signal Processing Toolbox 8.0, The MathWorks, Inc., Natick, Massachusetts, United States).

#### 2.4. PWV evaluation from time-delay curves

After the determination of the transit time of a pulse in the aorta, PWV can be locally determined as the inverse of the slope at each position. For in-vivo studies, some reports as [35], have described the effect of the reflections in the quality of PWV estimations. The evaluation of the advancing pulse is affected by complex morphology, sudden variations in wall stiffness, thickness or cross-section diameters, and asynchronous movements of surrounding organs may lead to local flow alterations, leading to backward waves and eventually some vortexes [36].

To determine only forward pulses, we proposed the following procedure to estimate PWV: (a) Determined sections having a similar trend (with the Pruned Exact Linear Time algorithm, or PELT, proposed by [37] using six segments as maximum), (b) Fit each section with a polynomial interpolation, and (c) Negative slopes were neglected. In Fig. 2, the time-delay was decomposed in independent sections automatically detected using the Matlab implementation of PELT algorithm, using the findchangepts function. Then, each section was fitted using a polynomial of degree 2.

#### 2.5. PWV from 3D fluid-structure simulations

To evaluate the method, a 3D FSI model, following [38–40], was used to provide synthetic data to calculate PWV. The geometry used in the simulations is described in Fig. 3, and the FSI Model is explained in the appendix section.

Using the information provided in the FSI model and evaluating the more precise solution to Moens-Korteweg relation (e.g. [21] for wave speed (see [41], PWV can be calculated as

$$PWV = \phi \left( \frac{K_f}{\rho_f} \right)^{\frac{1}{2}} \left( 1 + \left[ \frac{(D+2h)^2}{h(D+h)} - 2(1-\nu) \right] \frac{K_f}{E} \right)^{-1/2} \approx 477.2 \frac{[cm]}{[s]} \quad (4)$$

with  $\phi = \left( 1 - \nu^2 \left( 1 + \frac{Eh}{K_f D} \left( 1 - \frac{K_f \rho_s}{E \rho_f} \right) \right) \right) \approx 0.94$  and Bulk modulus  $K_f = 2.2 \times 10^{10} \left[ \frac{dyn}{cm^2} \right]$  for water.

#### 2.6. PWV evaluation using patients and volunteer's data

We used 4D-Flow MRI data previously acquired from a population of 18 adult volunteers ( $30.40 \pm 6.32$  years old, BMI  $23.31 \pm 6.52$ , 10 men), a cohort of 5 young volunteers ( $3.6 \pm 1.7$  years old, BMI  $20.5 \pm 5.6$ ), and 8 Fontan patients that have undergone surgery involving the reconstruction of the proximal aorta, with the placement of a Goretex patch in the ascending and transverse aorta (age:  $7.7 \pm 2.5$  years old, BMI  $16.5 \pm 1.6$ ). Typically, the reconstructed aorta in these patients is characterized by dilatation of the proximal part with tapering over the transverse arch (see [42]).

Parameters of the 4D-Flow sequence included retrospective cardiac gating, 25 cardiac phases, reconstructed voxel size of 2–2.5 mm isotropic targeted to the patient size, and  $TR(ms)/TE(ms) = 4.8/2.7$ . After that, 100 equidistant isosurfaces are considered for the calculations of local PWV.

For each subject, the distance along the aorta was normalized between 0 and 1 by dividing by its maximum value. In this way, we compared different morphologies, after removal of upper branches in all subjects.

To compare groups, boxplots and mean/standard deviation/median PWV values were estimated for each group. We used the Wilcoxon signed-rank test to evaluate statistical differences at different sections in the aorta, namely, the ascending aorta (AAo), the aortic arch (AArch), the proximal descending aorta (pDAo), and the distal descending aorta (dDAo). Additionally, global PWV was calculated in the entire thoracic aorta using two methods for each group: the slope of the linear regression in time-delay plots as proposed in [9], and the average of the continuous PWV obtained with our method, including Wilcoxon signed-rank test.

### 3. Results

As described in the previous section, the application of a geodesic distance also defines a map that allows the localization of the calculated PWV at each position along the aorta. We take advantage of that to identify coordinates in the mesh corresponding to positions along the aorta, enabling the visualization of results on the corresponding morphology.

#### 3.1. Fluid-Structure simulation

In Fig. 4, the comparison between straight and bent pipes describes how morphology affects the evaluation of PWV. In this case, the mesh, the geodesic, and the PWV map are shown in Fig. 4a, 4b and 4c, respectively. Fig. 4d incorporates the flow chart for the bent (top-left) and straight (top-right) pipes, and the PWV evaluation along the respective pipes (bottom). Following peak values in the flow chart reveal local variations due to the presence of the arch in the bent pipe.

Equation (4) provides a theoretical value of 477.2 [cm/s] for the straight pipe, which can be used as a reference. In that case, the evaluation with our method produces a constant PWV of 427.7 [cm/s], representing an underestimation of 10.4 %. In contrast, the bent pipe describes a softening before the arch (before  $d = 1.5$  in Fig. 4b, reaching a minimum of 200 [cm/s] in the arch and approaching 600 [cm/s] in the descending part. The effect of the morphology is noticeable, showing a decreased PWV in the arch compared to the rest of the pipe. Despite that variation, the average is 426.9 [cm/s]; this is an underestimation of 10.5 % with respect to the reference given for straight pipes.

For comparison purposes, different approaches were also

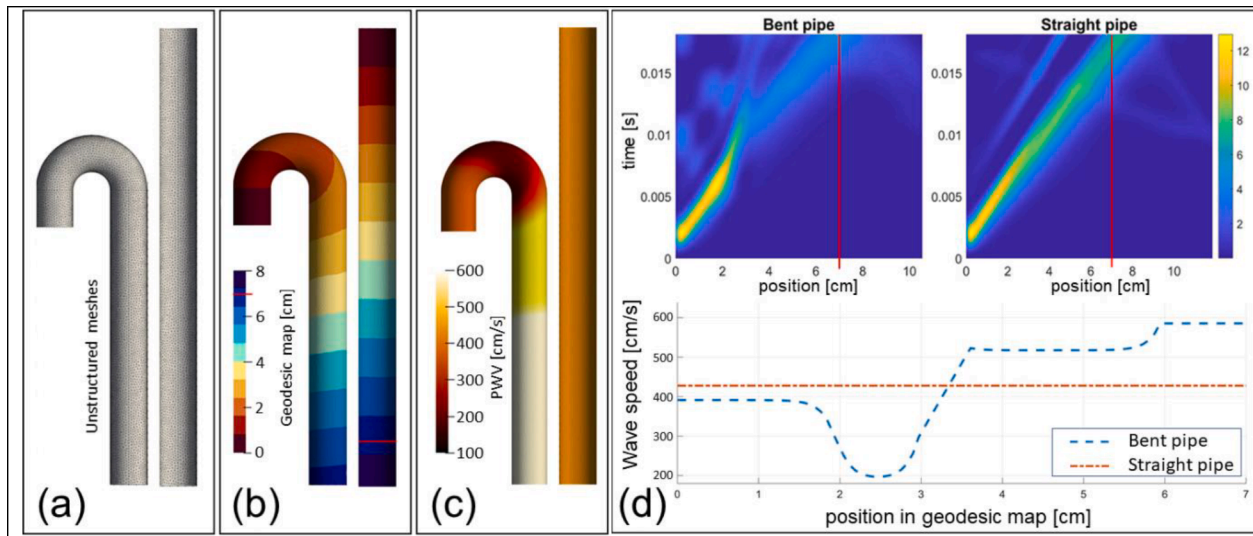


**Fig. 4.** Bent and straight pipes: the mesh (a), the geodesic map (b), and the projection of PWV estimation from 1D to 3D in (c). The figure (d) top-left indicates Flow in bent pipe evaluated at different positions and time. Figure (d) top-right: Flow in straight pipe evaluated at different positions and time. Figure (d) bottom: PWV calculated at each position for both geometries. The positions denoted in the x-axis of figure (d) corresponds to the map conceived with the geodesic map given in (b).

implemented. The methods compare the flow curves between the inlet and a plane located at 6.5 [cm] from the inlet, namely first-last, then the evaluation of the inverse slope calculated from the linear regression in the time-delay curve (see [9]), and the average PWV calculated along the centerline with our method. The results are shown in Table 1, showing, in general, a good agreement, where the First-Last and Linear-Regression methods have a better performance, indicating a difference below 4 %, with respect to the theoretical value found with equation (4). In comparison, our method has an underestimation of approximately 10 % for the same reference. In contrast, our global average of PWV was closer to the theoretical one than other methods (10.5 % versus 14.2 % and 17.3 %) for the bent pipe. Moreover, our result is consistent with the average for the straight tube with the same method.

### 3.2. Volunteers and patients using MRI data

Examples of local PWV evaluations for an adult volunteer, a young volunteer, and a Fontan patient are shown in Fig. 5a, 5b, and 5c, respectively. The evaluation of PWV was separated into four sections, considering all subjects per group in boxplots in Fig. 5d and 5e. These sections were defined, for each subject, as ascending aorta (AAo), aortic arch (AArch), proximal descending aorta (pDAo) and distal descending aorta (dDAo).

In Table 2, the mean PWV value, standard deviation, and median were estimated for different groups at different sections in the aorta for volunteers and patients. The comparisons consider the pairs volunteers (young and adult) and equivalent subjects (young volunteer and patient) because the groups of patients are children, not adults.

Young and adult volunteers showed the same trend in different sections in the aorta. A reduction in PWV was observed in the aortic arch in both groups in comparison to other regions, similarly as in the FSI

simulation. A consistent increment in PWV for adults compared to young volunteers (mean ages are 30.4 and 13.6 years old, respectively) presented significant differences in all regions ( $p < 0.01$ ).

The comparison between Fontan patients and young volunteers showed that Fontan patients had an increased PWV value in the aortic arch (5.63 [m/s] compared to 2.09 [m/s], representing an increment of 269 % in the mean value). The Wilcoxon rank test only shows statistical differences in the aortic arch, corresponding to the intervention area in Fontan patients.

In Fig. 6, the global PWV is evaluated along the entire thoracic aorta using (a) the slope of the linear regression in time-delay plots as proposed in [9], and (b), the average of the continuous PWV obtained with our method. Significant differences were found only between young and adults groups ( $p < 0.01$ ), showing equivalent trends using the linear regression method and the average of our continuous result.

## 4. Discussion

Since PWV is a consequence of the interplay between geometry, stiffness, and thickness, it is clinically relevant to reveal local features about the structure using non-invasive measurements. We achieved this goal by using a geometric optics argument (the Eikonal problem) to describe the shape of wavefronts along the arteries. To our knowledge, this approach has not been previously considered.

The automatic distance measured along the artery facilitates the evaluation of flow at any position, without centerlines, and avoids overlapping flow surfaces (see, e.g. [3]), all calculated at a low computational cost. After the segmentation of MR images, the overall processing time was in the order of 1 min. Additionally, the distance map enables projecting the result onto three-dimensional morphologies for better visualization.

**Table 1**

PWV values and its differences with respect to the reference value applying equation (4). In the first and third column, PWV is calculated using cross-correlation between first and last flow curves (First-Last), the inverse of the slope using linear regression in time-delay plot (Linear Regression), and the average of the continuous PWV values along the artery with the proposed method (Average). The difference in the second and fourth columns is indicated as percentages, and all of them are below that reference.

Method	PWV Straight tube [cm/s]	Difference wrt (4) (straight)	PWV Bent tube [cm/s]	Difference wrt (4) (bent)
First-Last	461.1	3.4 %	394.8	17.3 %
Linear Regression	458.8	3.9 %	409.4	14.2 %
Average	427.7	10.4 %	426.9	10.5 %

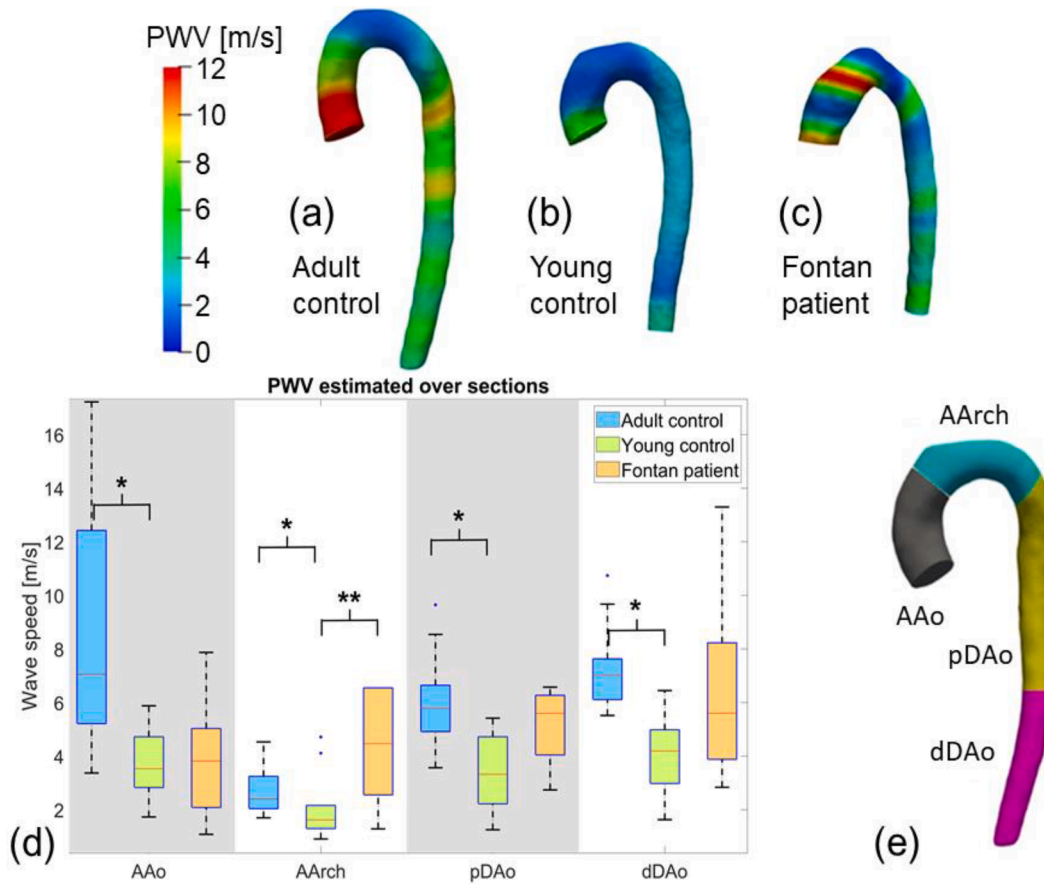


Fig. 5. PWV values projected onto 3D meshes for (a) an Adult volunteer, (b) a Young volunteer and (c) a Fontan patient. Boxplots in (d) with the PWV values obtained for three different groups: Healthy adult controls (cyan), Healthy young control (green) and Patients after Fontan procedure (orange). The definition of the sections is shown in (e).

Table 2

Mean, standard deviation, and median values obtained for Young controls, Adult controls, and Fontan patients measured at four sections, including marks for statistical differences between groups. These sections are denoted as ascending aorta (AAo), aortic arch (AArch), proximal descending aorta (pDAo), and distal descending aorta (dDAo), respectively.

	AAo	AArch	pDAo	dDAo		
Mean Young	3.70	*	2.09	*,**	3.38	*
Std Young	1.29		1.28		1.41	1.42
Median Young	3.53		1.62		3.32	4.19
Mean Adult	9.41	*	2.71	*	6.13	*
Std Adult	5.64		0.90		1.56	1.46
Median Adult	7.05		2.40		5.78	7.02
Mean Fontan	3.88		5.63	**	4.79	8.05
Std Fontan	2.22		5.77		1.62	5.20
Median Fontan	3.80		4.47		5.53	5.64

The differences observed of PWV in Table 1 for straight pipe, the First-Last and Linear Regression approaches show a better performance than ours with respect to the reference of 477.2 [cm/s] (3.4 % and 3.9 %, resp. and ours 10.4 %), calculated using the equation (4). However, considering the full simulated pipe, our method seems to be more stable (10.5 % of difference) for straight and bent pipes, while the other techniques present more significant variations (17.3 % and 14.2 %, resp.). In that sense, the application of First-Last and Linear Regression methods would identify as different the straight and bent pipes for the same material, thickness, and diameter, but could not identify the location of its difference. Further, in our numerical simulations, the PWV value for the bent pipe is not constant along the artery (see Fig. 4d

around the value obtained in a straight pipe, being consistent with previous reports [29,43], where the effect of the curvature produces a diminished PWV value in the arch, which increases towards the outlet. Although these findings could shed some light on the relation between PWV and morphology, additional studies are required to assess global sensibility regarding morphologic variations and noise.

In the in-vivo data from young and adult volunteers, a consistent decrement in PWV values is observed in the aortic arch, from the ascending to the descending aorta. That is similar to findings in previous reports. In [44], the aorta in adults was studied in 4 sections, from the arch to the thoracic aorta, showing that the aortic arch was slightly less stiff than the descending aorta. In [45], a combination of techniques shows that PWV is slightly lower in the aortic arch than the ascending aorta. To compare with other results (from Table 2 in [45] and using manual positioning of planes), PWV for the AArch is in the order of  $3.84 \pm 0.75$  [m/s], AAo  $4.59 \pm 1.11$  [m/s], and DAo  $5.22 \pm 1.22$  [m/s] for healthy subjects below 50 years old (AArch were obtained with regional aortic arch MRI while AAo and DAo were obtained with distensibility measures.) Our comparable PWV values from boxplots are for adult subjects AArch 2.4 [m/s], AAo 7.1 [m/s], pDAo 5.8 [m/s] and dDAo 7.0 [m/s], being consistent with the inferior value for the aortic arch.

The sample size of our healthy young controls (children) was small compared to adult controls due to the difficulty in recruiting them for a 4D-Flow MRI study. Nevertheless, the comparison between young and adult volunteers showed increasing values of PWV with age, which were consistent with previous analyses (see [9,12,45–46]; due to an increased stiffening of aortic walls as the age increases.

Interesting results in the comparison of young volunteers and Fontan

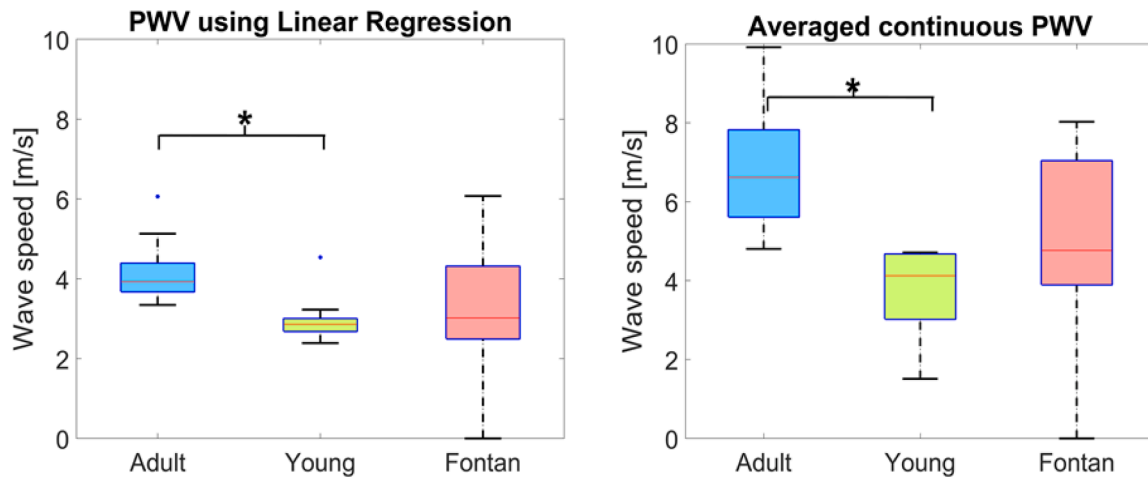


Fig. 6. Comparison of PWV values calculated along the full artery for each group. *Left*: Using the slope of the linear regression in successive time-delay curves, following Markl et al. (2010) [9]. *Right*: Average PWV calculated along the artery length using the proposed method.

patients were shown in 5(d) and Table 2. Since the ages were similar, it was also expected to obtain comparable values in several parts of the aorta. However, in Fontan patients, the PWV in the aortic arch was higher than in young volunteers and adults. This elevated PWV was probably due to surgical aortic arch reconstruction as these patients underwent in their early life, which might significantly alter local mechanical properties (due to the insertion of Goretex patches) and shape (tapering from the ascending aorta) (see [42] and references therein). This result showed the potential of our technique to identify alterations through continuous PWV.

The comparison in Fig. 6 was consistent with findings reported by [9], where global evaluations in adult volunteers showed higher PWV values than young volunteers, and there, for both methods, we detect significant differences. However, there was no statistically significant difference with Fontan patients, possibly related to the small sample size.

One aspect addressed in this work, was the occurrence of localized negative slopes in time-delay curves, which may seem contrary to the causality principle, i.e., with the advance of the wavefront, the time-delay monotonically increases as we move away from the inlet. From visual inspection of 4D-Flow MRI data, rapid alterations, or flow disorders concentrated at some specific positions in the aorta, occurring in a few time frames, produce that negative slope. In [35], bias effects in the evaluation of time-delays due to the “confluence of incident and reflected waves” have also been reported. We hypothesize that rapid variations in the morphology or wall stiffness, turbulent flow or vortices, or the influence of the movement of organs in contact with the aorta may introduce alterations in PWV evaluations. Those events might produce sharp (but localized) bias in the time delay and require more depth exploration.

The resolution of three-dimensional vector data recovered in the full aorta compromised the temporal resolution and scanning times. That has to be taken into account to avoid significant inaccuracies in evaluating time delays [47]. In that direction, some improvements have been proposed as multislice 2D Phase-Contrast scanning with one-dimensional velocity encoding (see, e.g. [48] or 2D PC with M-mode Fourier velocity encodings [49]. Those techniques can produce high-quality time delay curves by manual co-location of planes in the aorta, extending the patient’s time inside the scanner, or at the expense of evaluating only PWV in the descending aorta. In our case, we proposed Fourier-based curve fitting and perturbations in the data to produce robust time delay estimations. We obtained the cross-correlation taking all the possible combinations among Fourier coefficients and the data perturbations. Another limitation in our study is that the segmentation of the aorta is fixed, i.e., omitting the movement of the aorta. That is

related to the resolution of 4D-Flow MRI (in the order of 2–2.5 mm), which is not enough to assert the movement of the arterial wall in the entire image during the cardiac cycle. Fortunately, the velocity near the walls in the aorta is remarkably reduced. Therefore, its contribution to the evaluation of flows was negligible.

## 5. Conclusion

This paper proposed a novel method to efficiently construct a PWV map along the entire thoracic aorta using 4D flow MRI data from in vitro and in vivo data. No manual plane placements or centerlines were required. The methodology provided a promising non-invasive and semi-automatic technique to obtain local information about the aortic wall properties that apply to several cardiovascular diseases. Our initial results show not only the convenience of local analyses but also the relevance of the geometry as in the aortic arch, where PWV is lower for both FSI simulations and in vivo data. This work suggests new research questions about the relevance of the morphology in the evaluation of PWV in large vessels and how that may be related to internal reflections for pulsatile flows. The application of our method to arteries and their branches, like those in the carotid, is also a subject of future work.

## CRediT authorship contribution statement

**Joaquín Mura:** Conceptualization, Formal analysis, Investigation, Software, Writing – original draft, Writing – review & editing. **Julio Sotelo:** Formal analysis, Data curation, Investigation, Software, Visualization, Writing – original draft, Writing – review & editing. **Hernán Mella:** Investigation, Writing – original draft, Writing – review & editing. **James Wong:** Data curation, Writing – review & editing. **Tarique Hussain:** Supervision, Methodology. **Bram Ruijsink:** Investigation, Data curation, Funding acquisition, Writing – review & editing. **Sergio Uribe:** Supervision, Conceptualization, Funding acquisition, Resources, Writing – review & editing.

## Declaration of Competing Interest

The authors declare that they have no known competing financial interests or personal relationships that could have appeared to influence the work reported in this paper.

## Acknowledgment

This publication was funded by ANID - Millennium Science Initiative Program – NCN17\_129. Also, has been supported by FONDECYT

Postdoctorado #3170737, the ANID Ph.D. Scholarship #21170592, and ANID FONDECYT de Iniciación en Investigación #11200481, ANID

FONDECYT #1181057, and Initiation-Reactivation USM project PI\_LII\_2021\_86.

## Appendix

### A. The FSI Model

The implementation uses strong coupling between Navier-Stokes in Arbitrary Lagrangian-Eulerian formulation (ALE) with the Saint-Venant finite elasticity model for the solid wall. The simulations were performed with a homemade FSI coded in Python with the DOLFIN 2017.2.0 (FEniCS) package [50], delivering the data to evaluate PWV. A straight pipe and a bent pipe using the same coefficients for the solid, this is, the Young modulus of  $E = 3 \times 10^6 \left[ \frac{\text{dyn}}{\text{cm}^2} \right]$ , Poisson's ratio  $\nu = 0.3$ , inner diameter  $D=1[\text{cm}]$  and wall thickness  $h=0.1[\text{cm}]$ . The fluid density was  $\rho_f = 1 \left[ \frac{\text{gr}}{\text{cm}^3} \right]$  and  $\rho_s = 2 \left[ \frac{\text{gr}}{\text{cm}^3} \right]$  stands for the solid density.

For the straight pipe, the unstructured mesh consisted of 19717 nodes and 97393 tetrahedra for the fluid mesh. The solid mesh was composed of 17802 nodes and 55751 tetrahedra in a total length of 12 [cm]. In the case of the bent pipe, the curvature radius along the axis symmetry was 1 [cm], and its total length (measuring its centerline) coincides with that of the straight pipe. The fluid mesh was composed of 19106 nodes and 92701 tetrahedral elements, and the solid mesh contained 18127 nodes and 56944 tetrahedra.

The fluid used a Taylor-Hood finite element, and the polynomial space for the solid was the Lagrange quadratic elements. At the inlet, a velocity profile was imposed, following [51] (Eq. (5.14)), given by  $u_{in}(r, t) = 343.99(0.25 - r)^2(-1357t^9 + 7433t^8 - 17099t^7 + 21255t^6 - 15356t^5 - 6379t^4 - 1368t^3 + 97t^2 + 6t)$  where  $r$  was the local radial coordinate at the inlet and  $t$  the time evolution. The condition applied at the outlet was a do-nothing type

## References

- [1] C.A. Taylor, T.A. Fonte, J.K. Min, Computational fluid dynamics applied to cardiac computed tomography for non-invasive quantification of fractional flow reserve: Scientific basis, *J. Am. Coll. Cardiol.* 61 (22) (2013) 2233–2241, <https://doi.org/10.1016/j.jacc.2012.11.083>.
- [2] Z. Gao, X. Wang, S. Sun, D. Wu, J. Bai, Y. Yin, X. Liu, H. Zhang, V.H.C. de Albuquerque, Learning physical properties in complex visual scenes: An intelligent machine for perceiving blood flow dynamics from static CT angiography imaging, *Neural Networks*. 123 (2020) 82–93. [10.1016/j.neunet.2019.11.017](https://doi.org/10.1016/j.neunet.2019.11.017).
- [3] M. Markl, A. Frydrychowicz, S. Kozerke, M. Hope, O. Wieben, 4D flow MRI, *J. Magn. Reson. Imaging*. 36 (5) (2012) 1015–1036, <https://doi.org/10.1002/jmri.v36.5.10.1002/jmri.23632>.
- [4] P. Dyverfeldt, M. Bissell, A.J. Barker, A.F. Bolger, C.J. Carlhäll, T. Ebbers, C. J. Francios, A. Frydrychowicz, J. Geiger, D. Giese, M.D. Hope, P.J. Kilner, S. Kozerke, S. Myerson, S. Neubauer, O. Wieben, M. Markl, 4D flow cardiovascular magnetic resonance consensus statement, *J. Cardiovasc. Magn. Reson.* 17 (2015) 1–19, <https://doi.org/10.1186/s12968-015-0174-5>.
- [5] N.S. Burris, M.D. Hope, 4D Flow MRI Applications for Aortic Disease, *Magn. Reson. Imaging Clin. N. Am.* 23 (1) (2015) 15–23, <https://doi.org/10.1016/j.mric.2014.08.006>.
- [6] E.E. Calkoen, A.A.W. Roest, R.J. Van Der Geest, A. De Roos, J.J.M. Westenberg, Cardiovascular function and flow by 4-dimensional magnetic resonance imaging techniques: New applications, in: *J. Thorac. Imag. Lippincott Williams Wilkins* (2014) 185–196, <https://doi.org/10.1019/RTI.0000000000000068>.
- [7] J. Sotelo, J. Urbina, I. Valverde, J. Mura, C. Tejos, P. Irarrazaval, M.E. Andia, D. E. Hurtado, S. Uribe, Three-dimensional quantification of vorticity and helicity from 3D cine PC-MRI using finite-element interpolations, *Magn. Reson. Med.* (2017), <https://doi.org/10.1002/mrm.26687>.
- [8] J. Sotelo, L. Dux-Santoy, A. Guala, J. Rodríguez-Palomares, A. Evangelista, C. Sing-Long, J. Urbina, J. Mura, D.E. Hurtado, S. Uribe, 3D axial and circumferential wall shear stress from 4D flow MRI data using a finite element method and a laplacian approach, *Magn. Reson. Med.* 79 (2018), <https://doi.org/10.1002/mrm.26927>.
- [9] M. Markl, W. Wallis, S. Brendecke, J. Simon, A. Frydrychowicz, A. Harloff, Estimation of global aortic pulse wave velocity by flow-sensitive 4D MRI, *Magn. Reson. Med.* 63 (6) (2010) 1575–1582, <https://doi.org/10.1002/mrm.22353>.
- [10] A. Wentland, T. Grist, O. Wieben, Review of MRI-based measurements of pulse wave velocity: a biomarker of arterial stiffness, *Cardiovasc. Diagn. Ther.* 2 (2014) 193–206, <https://doi.org/10.3978/j.issn.2223-3652.2014.03.04>.
- [11] Y.C. Fung, in: *Biomechanics*, Springer New York, New York, NY, 1990, pp. 1–28, [https://doi.org/10.1007/978-1-4419-6856-2\\_1](https://doi.org/10.1007/978-1-4419-6856-2_1).
- [12] M.C. Whitlock, W.G. Hundley, Noninvasive Imaging of Flow and Vascular Function in Disease of the Aorta, *JACC Cardiovasc. Imaging*. 8 (9) (2015) 1094–1106, <https://doi.org/10.1016/j.jcmg.2015.08.001>.
- [13] M.F. O'Rourke, A. Adji, An updated clinical primer on large artery mechanics: Implications of pulse waveform analysis and arterial tonometry, *Curr. Opin. Cardiol.* 20 (2005) 275–281, <https://doi.org/10.1097/01.hco.0000166595.44711.6f>.
- [14] P. Salvi, A. Grillo, G. Parati, Non-invasive estimation of central blood pressure and analysis of pulse waves by applanation tonometry, *Hypertens. Res.* 38 (10) (2015) 646–648, <https://doi.org/10.1038/hr.2015.78>.
- [15] N. Westerhof, N. Stergiopoulos, M.I.M. Noble (Eds.), *Snapshots of Hemodynamics*, Springer US, Boston, MA, 2010.
- [16] T. Pereira, C. Correia, J. Cardoso, Novel methods for pulse wave velocity measurement, *J. Med. Biol. Eng.* 35 (5) (2015) 555–565, <https://doi.org/10.1007/s40846-015-0086-8>.
- [17] J. Calabria, P. Torguet, M. Garcia, I. Garcia, N. Martin, B. Guasch, D. Faur, M. Vallés, Doppler ultrasound in the measurement of pulse wave velocity: Agreement with the Complior method, *Cardiovasc. Ultrasound*. 9 (2011) 1–6, <https://doi.org/10.1186/1476-7120-9-13>.
- [18] B. Jiang, B. Liu, K.L. McNeill, P.J. Chowienzyk, Measurement of Pulse Wave Velocity Using Pulse Wave Doppler Ultrasound: Comparison with Arterial Tonometry, *Ultrasound Med. Biol.* 34 (3) (2008) 509–512, <https://doi.org/10.1016/j.ultrasmedbio.2007.09.008>.
- [19] D.J. Kortweg, Ueber die Fortpflanzungsgeschwindigkeit des Schalles in elastischen Röhren, *Ann. Phys.* 241 (12) (1878) 525–542, [https://doi.org/10.1002/\(ISSN\)1521-388910.1002/andp.v241:1210.1002/andp.18782411206](https://doi.org/10.1002/(ISSN)1521-388910.1002/andp.v241:1210.1002/andp.18782411206).
- [20] A.I. Moens, *Die Pulscurve*, E.J. Brill, Leiden, 1878.
- [21] W.W. Nichols, M.F. O'Rourke, C. Vlachopoulos, D.A. McDonald, McDonald's blood flow in arteries: theoretical, experimental and clinical principles., Hodder Arnold, 2011. <https://www.crcpress.com/McDonalds-Blood-Flow-in-Arteries-Sixth-Edition-Theoretical-Experimental/Vlachopoulos-O'Rourke-Nichols/p/book/9780340985014> (accessed August 21, 2018).
- [22] J.M. Boese, M. Bock, S.O. Schoenberg, L.R. Schad, Estimation of aortic compliance using magnetic resonance pulse wave velocity measurement, *Phys. Med. Biol.* 45 (2000) 1703, <http://stacks.iop.org/0031-9155/45/i=6/a=320>.
- [23] H.B. Grotenhuis, J. Ottenkamp, D. Fontein, H.W. Vliegen, J.J.M. Westenberg, L.J. M. Kroft, A. de Roos, Aortic elasticity and left ventricular function after arterial switch operation: MR imaging—initial experience, *Radiology* 249 (2008) 801–809, <https://doi.org/10.1148/radiol.2492072013>.
- [24] E.S.J. Kröner, R.J. van der Geest, A.J.H.A. Scholte, L.J.M. Kroft, P.J. van den Boogaard, D. Hendriksen, H.J. Lamb, H.-M. Siebelink, B.J.M. Mulder, M. Groenink, T. Radonic, Y. Hillhorst-Hofstee, J.J. Bax, E.E. van der Wall, A. de Roos, J.H. C. Reiber, J.J.M. Westenberg, Evaluation of sampling density on the accuracy of aortic pulse wave velocity from velocity-encoded MRI in patients with Marfan syndrome, *J. Magn. Reson. Imaging*. 36 (6) (2012) 1470–1476, <https://doi.org/10.1002/jmri.v36.6.10.1002/jmri.23729>.
- [25] Geuzaine, Christophe and Remacle, Jean-Francois, Gmsh, (n.d.). <http://http://gmsh.info/>.
- [26] J. Bock, A. Frydrychowicz, A.F. Stalder, T.A. Bley, H. Burkhardt, J. Hennig, M. Markl, 4D phase contrast MRI at 3 T: Effect of standard and blood-pool contrast agents on SNR, PC-MRA, and blood flow visualization, *Magn. Reson. Med.* 63 (2) (2010) 330–338, <https://doi.org/10.1002/mrm.v63:210.1002/mrm.22199>.
- [27] Q. Fang, D.A. Boas, Tetrahedral mesh generation from volumetric binary and grayscale images, in: *Proc. - 2009 IEEE Int. Symp. Biomed. Imaging From Nano to Macro*, ISBI 2009, 2009; pp. 1142–1145. [10.1109/ISBI.2009.5193259](https://doi.org/10.1109/ISBI.2009.5193259).
- [28] A. van Engelen, M. Silva Vieira, I. Rafiq, M. Cecelja, T. Schneider, H. de Bliet, C. A. Figueroa, T. Hussain, R.M. Botnar, J. Alastruey, Aortic length measurements for pulse wave velocity calculation: manual 2D vs automated 3D centreline extraction, *J. Cardiovasc. Magn. Reson.* 19 (2017) 32, <https://doi.org/10.1186/s12968-017-0341-y>.
- [29] F. He, L.u. Hua, L.-J. Gao, Numerical simulation of pulse wave propagation in a curved artery, *J. Mech. Sci. Technol.* 31 (1) (2017) 473–478, <https://doi.org/10.1007/s12206-016-1051-3>.
- [30] P.G. Tucker, S.A. Karabasov, Unstructured grid solution of the eikonal equation for acoustics, (2009) 535–554.

- [31] J. Qian, Y.-T. Zhang, H.-K. Zhao, Fast Sweeping Methods for Eikonal Equations on Triangular Meshes, *SIAM J. Numer. Anal.* 45 (1) (2007) 83–107, <https://doi.org/10.1137/050627083>.
- [32] E.S. Ibrahim, K. Johnson, A. Miller, J. Shaffer, R. White, Measuring aortic pulse wave velocity using high-field cardiovascular magnetic resonance: Comparison of techniques, *J. Cardiovasc. Magn. Reson.* 12 (2010) 26, <https://doi.org/10.1186/1532-429X-12-26>.
- [33] A.L. Wentland, T.M. Grist, O. Wieben, Review of MRI-based measurements of pulse wave velocity: a biomarker of arterial stiffness, *Cardiovasc. Diagn. Ther.* 4 (2014) 193–206, <https://doi.org/10.3978/j.issn.2223-3652.2014.03.04>.
- [34] S. Zahedi, A.-K. Tornberg, Delta function approximations in level set methods by distance function extension, *J. Comput. Phys.* 229 (6) (2010) 2199–2219, <https://doi.org/10.1016/j.jcp.2009.11.030>.
- [35] E. Hermeling, K.D. Reesink, R.S. Reneman, A.P.G. Hoeks, Confluence of incident and reflected waves interferes with systolic foot detection of the carotid artery distension waveform, *J. Hypertens.* 26 (2008) 2374–2380, <https://doi.org/10.1097/HJH.0b013e328311cdd5>.
- [36] M.R. Najjari, M.W. Plesniak, Evolution of vortical structures in a curved artery model with non-Newtonian blood-analog fluid under pulsatile inflow conditions, *Exp. Fluids.* (2016), <https://doi.org/10.1007/s00348-016-2188-7>.
- [37] R. Killick, P. Fearnhead, I.A. Eckley, Optimal detection of change-points with a linear computational cost, *J. Am. Stat. Assoc.* 107 (500) (2012) 1590–1598, <https://doi.org/10.1080/01621459.2012.737745>.
- [38] S. Deparis, Numerical Analysis of Axisymmetric Flows and Methods for Fluid-Structure Interaction Arising in Blood Flow Simulation, Thesis. 2965 (2004) 144. <https://doi.org/10.5075/epfl-thesis-2965>.
- [39] M.A. Fernández, J.-F. Gerbeau, Algorithms for fluid-structure interaction problems, in: F. L., Q. A., V. A. (Eds.), *Cardiovasc. Math.*, Springer, Milano, Milano, 2009: pp. 307–346. [10.1007/978-88-470-1152-6\\_9](https://doi.org/10.1007/978-88-470-1152-6_9).
- [40] S. Gjertsen, Development of a Verified and Validated Computational Framework for Fluid-Structure Interaction: Investigating Lifting Operators and Numerical Stability, University of Oslo, 2017. <https://www.duo.uio.no/handle/10852/57788> (accessed March 31, 2020).
- [41] C.J. Greenshields, H.G. Weller, A unified formulation for continuum mechanics applied to fluid-structure interaction in flexible tubes, *Int. J. Numer. Methods Eng.* 64 (12) (2005) 1575–1593, [https://doi.org/10.1002/\(ISSN\)1097-020710.1002/nme.v64:1210.1002/nme.1409](https://doi.org/10.1002/(ISSN)1097-020710.1002/nme.v64:1210.1002/nme.1409).
- [42] C. Haller, D. Chetan, A. Saedi, R. Parker, G.S. Van Arsdell, O. Honjo, Geometry and growth of the reconstructed aorta in patients with hypoplastic left heart syndrome and variants, *J. Thorac. Cardiovasc. Surg.* 153 (6) (2017) 1479–1487.e1, <https://doi.org/10.1016/j.jtcvs.2017.02.011>.
- [43] H. Li, K. Lin, D. Shahmirzadi, FSI Simulations of Pulse Wave Propagation in Human Abdominal Aortic Aneurysm: The Effects of Sac Geometry and Stiffness, *Biomed. Eng. Comput. Biol.* 7 (2016) 25–36, <https://doi.org/10.4137/BECB.S40094>.
- [44] S.S. Hickson, M. Butlin, M. Graves, V. Taviani, A.P. Avolio, C.M. McEnery, I. B. Wilkinson, The Relationship of Age With Regional Aortic Stiffness and Diameter, *JACC Cardiovasc. Imaging.* 3 (12) (2010) 1247–1255, <https://doi.org/10.1016/j.jcmg.2010.09.016>.
- [45] A. Dogui, N. Kachenoura, F. Frouin, M. Lefort, A. De Cesare, E. Mousseaux, A. Herment, Consistency of aortic distensibility and pulse wave velocity estimates with respect to the Bramwell-Hill theoretical model: A cardiovascular magnetic resonance study, *J. Cardiovasc. Magn. Reson.* 13 (2011) 11, <https://doi.org/10.1186/1532-429X-13-11>.
- [46] I. Voges, M. Jerosch-Herold, J. Hedderich, E. Pardun, C. Hart, D.D. Gabbert, J. H. Hansen, C. Petko, H.-H. Kramer, C. Rickers, Normal values of aortic dimensions, distensibility, and pulse wave velocity in children and young adults: a cross-sectional study, *J. Cardiovasc. Magn. Reson.* 14 (2012) 77, <https://doi.org/10.1186/1532-429X-14-77>.
- [47] K. Dorniak, E. Heiberg, M. Hellmann, D. Rawicz-Zegrzda, M. Wesierska, R. Galaska, A. Sabisz, E. Szurowska, M. Dudziak, E. Hedström, Required temporal resolution for accurate thoracic aortic pulse wave velocity measurements by phase-contrast magnetic resonance imaging and comparison with clinical standard applanation tonometry, *BMC Cardiovasc. Disord.* 16 (2016) 110, <https://doi.org/10.1186/s12872-016-0292-5>.
- [48] J.J.M. Westenberg, A. de Roos, H.B. Grotenhuis, P. Steendijk, D. Hendriksen, P. J. van den Boogaard, R.J. van der Geest, J.J. Bax, J.W. Jukema, J.H.C. Reiber, Improved aortic pulse wave velocity assessment from multislice two-directional in-plane velocity-encoded magnetic resonance imaging, *J. Magn. Reson. Imaging.* 32 (5) (2010) 1086–1094, <https://doi.org/10.1002/jmri.22359>.
- [49] V. Taviani, A.J. Patterson, M.J. Graves, C.J. Hardy, P. Worters, M.P.F. Sutcliffe, J. H. Gillard, Accuracy and repeatability of fourier velocity encoded M-mode and two-dimensional cine phase contrast for pulse wave velocity measurement in the descending aorta, *J. Magn. Reson. Imaging.* 31 (5) (2010) 1185–1194, <https://doi.org/10.1002/jmri.v31:510.1002/jmri.22143>.
- [50] A. Logg, G.N. Wells, DOLFIN: Automated finite element computing, *ACM Trans. Math. Softw.* 37 (2) (2010) 1–28, <https://doi.org/10.1145/1731022.1731030>.
- [51] G. Pena, Spectral element approximation of the incompressible Navier-Stokes equations in a moving domain and applications, EPFL (2009), <https://doi.org/10.5075/epfl-thesis-4529>.